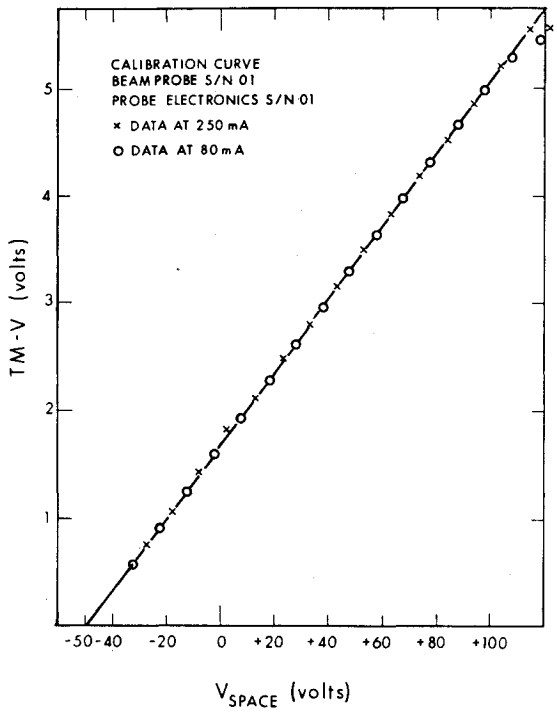

Fig. 2 Beam probe calibration curve.

smaller than those in the ionospheric plasma, the shield can operate up to several volts negative with respect to the emitter without introducing appreciable error. A slightly negative potential on the shield is desirable to prevent "stripping" electrons from the beam plasma, since it automatically limits the electron current collected to the ion current striking the shield.

The probe systems (Fig. 1, bottom) are designed to supply a constant current to heat the probe emitter and provide a means of determining the potential developed between the probe filament and spacecraft ground. The processed data from this potential measurement and the probe heater current are supplied to the spacecraft telemetry. The electronic configurations for the two probe systems are similar, but the beam probe system has an added transformer near the probe, and the ambient probe system has an added negative voltage power supply to provide the necessary bias voltage. The only other differences in the two systems are values of resistors and transformer windings due to the differences in heating requirements of the two different emitter designs. The calibration procedures for the two probe systems basically consisted of 1) stabilizing a plasma source at a desired ion density, 2) measuring the plasma potential at the "probe location" using a reference probe, 3) positioning the probe to be calibrated at the probe location, 4) recording the telemetry output voltage (TM-V) to establish the relationship between plasma potential and TM-V, and 5) recording TM-V for ambient probe bias voltages of $+50$v to -100v.

The ambient probe calibration was performed in a 5-ft-diam by 12-ft-long vacuum system, so that a low-energy argon ion source developed to calibrate plasma spectrometers such as the ALSEP and OGO instruments could be used to provide the low-density plasma necessary. From this calibration, the bias voltage of -50v was chosen.

The beam probe calibration was performed in a 2-ft-diam by 6-ft-long vacuum system. A 10-cm-diam mercury ion engine (supplied by NASA-Lewis Research Center) was used to generate the 3-kv ion beam. The 250-ma design current corrsponded to a density of $\sim 10^9$ ions/cm^3.

Typical calibration results for the beam probe system are shown in Fig. 2 and are accurate throughout the ion density and potential range of interest. The results for the ambient probe system are very similar but are subject to more doubt than for the beam probe because of sheath considerations in this density range. The validity of the calibration of the ambient probe may be demonstrated during the SERT-II flight when the spacecraft is forced to potential differences with respect to the space plasma.

An Improved High-Power Xenon Short-Arc Lamp

YOSHIHIKO NAKAMURA*
Ushio Electric Inc., Tokyo, Japan

Introduction

IN Japan the development of xenon short-arc lamps was initiated in 1957. By use of forced-air cooling, a 5-kw lamp was developed and put to use as a light source for large Cinelama projectors, solar simulators and arc-image furnaces. This Note describes development of 25-kw and 30-kw short-arc (12-mm gap) xenon lamps with liquid cooled electrodes (Fig. 1). The 20-kw xenon short-arc lamps with liquid-cooled electrodes have been introduced by Thouret, Lienhard, etc.[1-3]

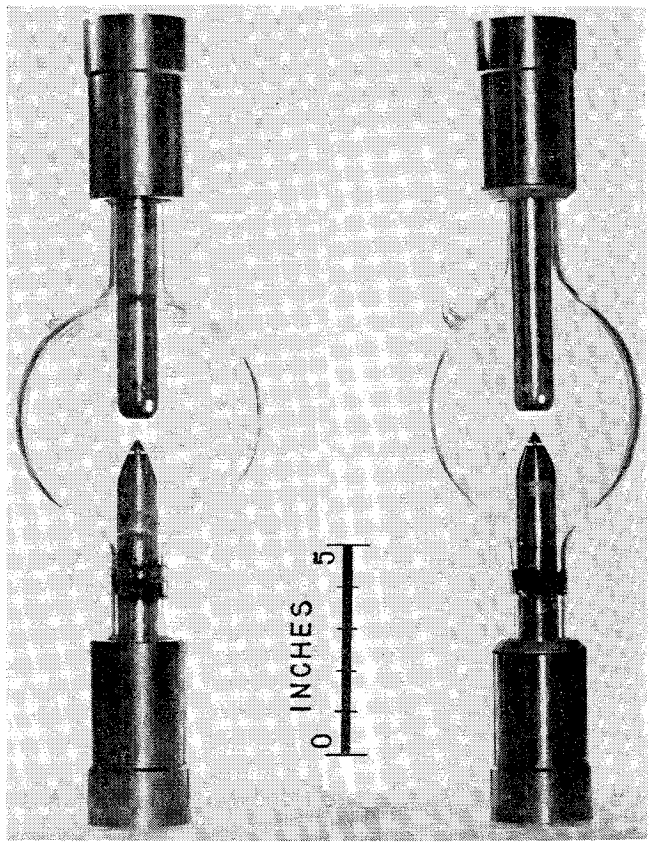

Fig. 1 Xenon 30-kw (left) and 25-kw (right) lamps.

Presented as Paper 69-998 at AIAA/ASTM/IES 4th Space Simulation Conference, Los Angeles, Calif., September 8, 1969; submitted September 18, 1969; revision received December 29, 1969.

* Research Engineer.

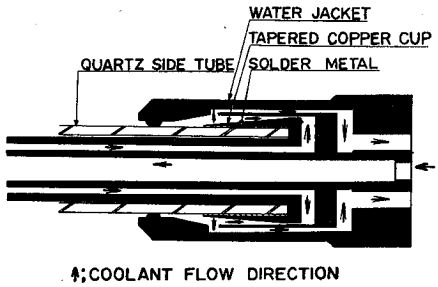

Fig. 2 Water cooled metal seal.

In our developmental study, emphasis was placed on 1) hermetic metal seals with high vibration-strength and unlimited shelf life, 2) liquid-cooled electrodes with enough heat dissipation capacity in order to overcome sputtering, melting, or deformation of electrodes, and 3) investigation of the lamp operating characteristics leading to the design of the most efficient and safe bulb.

Metal Seal

A soft soldering metal with a relatively low melting point ($\leq$400°F) has been found to provide a strong metal seal structure which can withstand up to 60-atm pressure with 30-mm-i.d. quartz tubes (Fig. 2). An additional liquid-cooled jacket is installed around the seal to prevent the seal from weakening during lamp operation. Unfavorable effects on the lamp performance due to this unusually low melting point of the seal have been eliminated by a) carefully degassing the liquid-cooled electrode mounts and b) using an alkaline-earth metal getter inside the lamp stem. The excellent antishock strength of the metal seal has been proved during a transportation test up to 40 g, and the reliability of the seals has been confirmed for at least 1 yr.

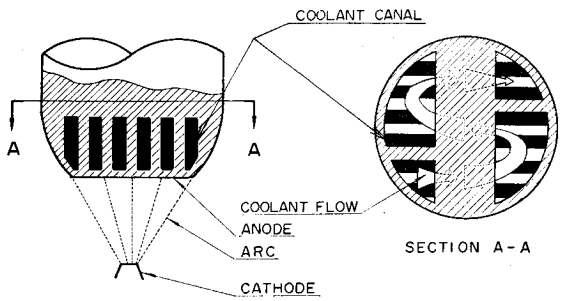

Fig. 3 Reciprocated fin type anode.

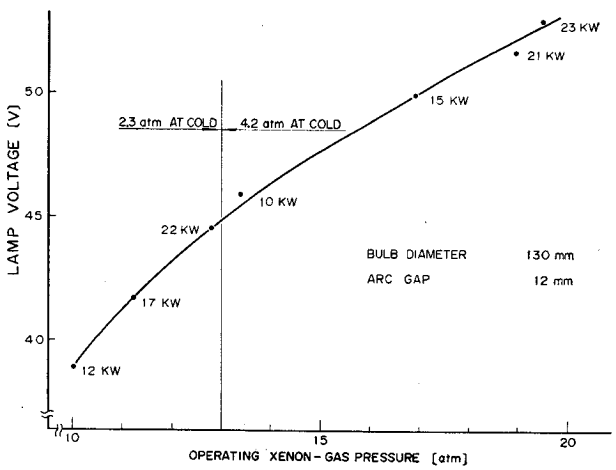

Fig. 4 Lamp voltage vs operating gas pressure.

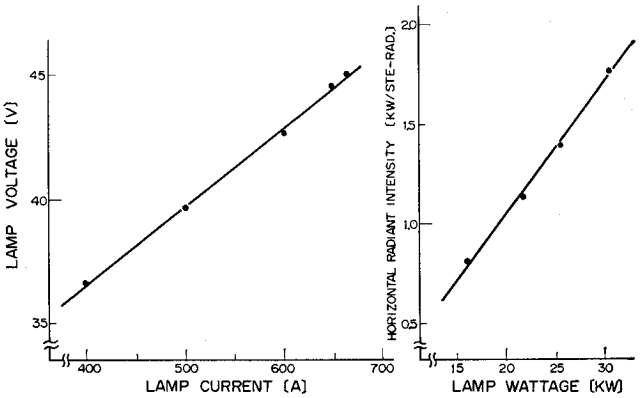

Fig. 5 Operating characteristics, 30-kw lamp.

Reciprocated-Fin-Type Anode

To improve the heat dissipation capacity of the liquid-cooled anode, the anode tip structure with a multiple-fin-type canal was developed. The deformation of the anode tip was

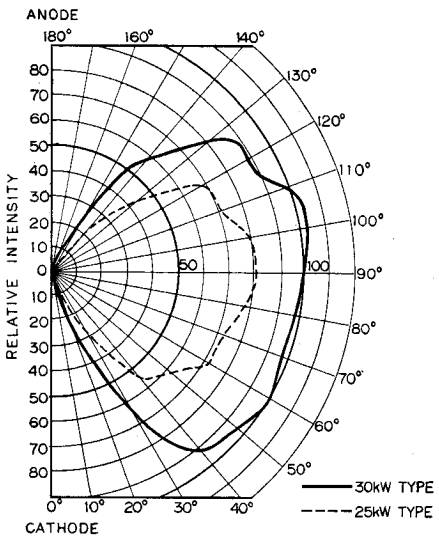

Fig. 6 Polar angular distribution, 25-kw and 30-kw lamps.

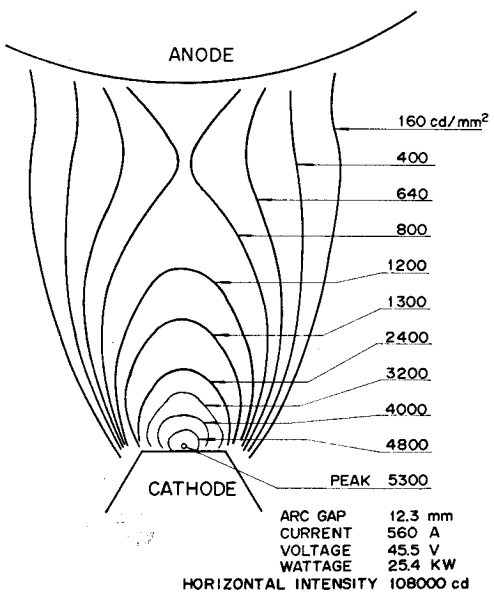

Fig. 7 Micro brightness distribution, 25-kw arc.

Table 1 Energy balance of a 25kw xenon lamp

	Energy, kw	%
Removed from anode	8.75	34.5
Removed from cathode	1.32	5.2
Removed by convection etc.	2.53	9.8
Radiated from arc	12.80	50.5
Total lamp input	25.40	100.0

completely avoided by this fin-type structure; however, the current capacity of the anode was not so much improved, and the anode required twice as much water flow as conventional ones. These defects of the fin-type anode are practically eliminated by adopting the multiple reciprocated-fin-type structure shown in Fig. 3. The sectional area of the center fin group is narrower than those of the either side, and the coolant flows in series through these three or more fin groups. Thus, at the center portion of the anode where the heat generation rate is high, the flow speed is high, and at the edge portions, the flow speed is relatively low. Utilizing this reciprocated-fin-type anode, the 25-kw and 30-kw lamps are developed which have enough anode heat dissipation capacity against sputtering, melting, or deformation of the anode under the rated maximum lamp inputs of 26 kw and 31 kw, respectively.

Operating Characteristics

Figure 4 shows the relation between xenon-gas pressure and lamp voltage in operation which is obtained by the test lamp with the same geometry as the 25-kw type and provided with pressure gauge. The fact that the two curves for 2.3 and 4.2 atm cold-gas pressures connect smoothly suggests that the lamp voltage depends only on the operating gas pressure but not on the lamp input. As a compromise to the contrary requirements for the lamp safety and the conversion efficiency, the average lamp voltage of 45 v, the operating xenon-gas pressure of 13 atm and the cold-gas pressure of 2.3 atm are selected for the lamps with arc gap of 12 mm from the data of Fig. 4.[4] The safety factors of the lamp bulbs for these operating conditions are estimated to be around 6.5 for operation and 80 for the cold condition, respectively. The 6.5 for operation is of the same order as the safety factors for conventional xenon short-arc lamps, which are widely used for movie projectors, but the 80 for the cold condition is much higher than those for conventional lamps, because of fairly low cold-gas pressure of 1.3 atm over normal.

The electric and radiation characteristics of the 25-kw and 30-kw lamps are shown in Figs. 5–7. Table 1 describes typical energy dissipation balance of a 25-kw arc lamp. As shown in the table, up to 50.5% of the energy conversion efficiency is obtained for 25.4-kw lamp input.

As a result of this developmental work, 25-kw and 30-kw xenon short-arc sources, as shown in Fig. 1, with at least 400 hr of service life are obtained.

References

[1] Thouret, W. E., "High-Brightness Xenon Lamps with Liquid-Cooled Electrodes," *Illuminating Engineering*, Vol. LX, No. 5, May 1965, p. 339.

[2] Leinhard, O. E., "Xenon Compact Arc Lamps with Liquid-Cooled Electrodes," *Illuminating Engineering*, Vol. LX, No. 5, May 1965, p. 348.

[3] Bartera, R. E., "Recent Solar Simulation Developments at the Jet Propulsion Laboratory," Research Report, Contract NAS 7-100, Jet Propulsion Lab., pp. 681–683.

[4] Thouret, W. E., "Tensile and Thermal Stresses in the Envelope of High Brightness High Pressure Discharge Lamps," *Illuminating Engineering*, Vol. LV, No. 5, May, 1960, p. 295.

Theoretical Penetration Mechanics of Multisheet Structures Based on Discrete Debris Particle Modeling

A. J. RICHARDSON*
Space Division of North American Rockwell, Downey, Calif.

Nomenclature†

a = area on surface of debris cloud associated with each particle
C = primary particle and first-sheet material property related to internal energy to cause fracture
d, d_c = diameters of primary and composite particles
d_1 = diameter of average particle in debris cloud
D = diameter of spherical debris cloud
D_h = diameter of hole in first sheet
E = peak internal energy in composite particle due to impact
E''' = peak internal energy per unit volume of composite particle
f = finite sheet factor
F = instantaneous force at primary particle and first-sheet interface
h = spacing between two sheets
$\bar{h}$ = sheet spacing cutoff
H_i = Brinell hardness of sheet i, kg/$\overline{mm}^2$
m_p = mass of incident primary particle
m_{p1} = mass of average particle in debris cloud
m_s = mass removed from first sheet by primary particle
n = number of particles in debris cloud
p_2 = penetration into second sheet; $p_{20} = p_2$ for $h = 0$ and/or $t_1 = 0$; $p_{21} = p_2$ for $h \geq \bar{h}$
s = distance between particles on surface of debris cloud
s = distance between leading particles on second-sheet impact
t_i = thickness of sheet i
$\bar{t}_2$ = minimum thickness of second sheet to resist perforation; $\bar{t}_{20} = \bar{t}_2$ for $h = 0$ and/or $t_1 = 0$; $\bar{t}_{21} = \bar{t}_2$ for $h \geq \bar{h}$
T = time after cloud expansion begins
$\hat{T}$ = time at which leading particles strike second sheet
V_c = velocity of center of debris cloud along X axis
$\hat{V}_{1X}$ = X component of velocity of leading particle in debris cloud
V_p = normal impact velocity of primary particle
V_{pp} = velocity of primary particle during impact
V_r = radial velocity of particles in debris cloud
V_s = velocity of material removed from first sheet during impact
X = distance cloud center has traveled
α = spacing factor for center impacts on second sheet
β = m_s/m_p
ϵ = ultimate room-temperature tensile strain of particle and first-sheet material (%)
γ = second-sheet material constant related to penetration resistance (use 0.367 for metals)
η = primary particle and first-sheet material property relating fracture energy to material temperature
ρ_p = density of primary particle
ρ = density of average particle of debris cloud
ρ_i = density of sheet i
θ = time between initial impact and formation of composite particle

Introduction

TO date, two approaches have been followed in developing penetration mechanics for multisheet meteoroid-protection systems: the theoretical approach, based upon gaseous

Presented as Paper 69-371 at the AIAA Hypervelocity Impact Conference, Cincinnati, Ohio, April 30–May 2, 1969; submitted June 16, 1969; revision received November 3, 1969. The research described was supported by North American Rockwell.

* Member of the Technical Staff, Structural Systems and Mechanisms, Research, Engineering, and Test.

† Units are in the gram, centimeter, second system unless otherwise noted.